Hypersonic Phononic Crystals

T. Gorishnyy,[1,*] C. K. Ullal,[1] M. Maldovan,[1,2] G. Fytas,[3,4] and E. L. Thomas[1,2]

[1]*Department of Materials Science and Engineering, Massachusetts Institute of Technology, Cambridge, Massachusetts 02139, USA*
[2]*Institute for Soldier Nanotechnologies, Massachusetts Institute of Technology, Cambridge, Massachusetts 02139, USA*
[3]*Max Planck Institute for Polymer Research, P.O. 3148, 55128 Mainz, Germany*
[4]*Department of Materials Science and Technology, University of Crete, and FORTH, P.O. 1527, 71110 Heraklion, Greece*

(Received 8 October 2004; published 22 March 2005)

In this Letter we propose the use of hypersonic phononic crystals to control the emission and propagation of high frequency phonons. We report the fabrication of high quality, single crystalline hypersonic crystals using interference lithography and show that direct measurement of their phononic band structure is possible with Brillouin light scattering. Numerical calculations are employed to explain the nature of the observed propagation modes. This work lays the foundation for experimental studies of hypersonic crystals and, more generally, phonon-dependent processes in nanostructures.

DOI: 10.1103/PhysRevLett.94.115501 PACS numbers: 62.30.+d, 61.46.+w, 62.65.+k, 63.22.+m

The concept of phonon management has importance for both basic science and applications, ranging from heat management to reduction of noise in electronic circuits, and enhanced acousto-optical interactions. The fundamental property of phononic crystals is the existence of special frequency regions—phononic band gaps—where no mechanical wave can propagate. Phononic band gaps have their origin in the destructive interference of multiply scattered waves in periodic structures. In the past, much attention has been focused on sonic (midgap frequency $\omega_g = 10^2$–10^3 Hz) and ultrasonic ($\omega_g = 10^4$–10^6 Hz) crystals [1–5], partially due to their promise for applications in acoustics, remote sensing, and medical diagnostics, but also because of experimental convenience. Elements of these crystals are macroscopic objects that can be manually assembled into various structures [3], while simple ultrasonic transmittivity measurements provide information about their phononic band gaps. Hypersonic crystals ($\omega_g = 10^9$–10^{12} Hz) are more difficult to fabricate and characterize because of their inherently smaller length scale. In the past, there have been relatively few investigations of hypersonic crystals [6–8]. However, such materials influence high energy phonons in a novel and powerful way, which opens a pathway for exploration of entirely new phenomena. First, the presence of phononic band gaps perturbs the phononic density of states, which impacts physical quantities such as thermal conductivity and heat capacity [9]. Second, since the lattice spacing of hypersonic crystals is comparable to the wavelength of light, they exhibit both phononic and photonic band gaps. Acousto-optical interactions result in intriguing effects, such as optical cooling [10], and shock-wave-mediated light frequency shifts [11], and suggest a novel way to create a number of acousto-optical devices, such as optical modulators and optically pumped acoustic oscillators [12].

We fabricate 2D hypersonic phononic crystals using interference lithography [13,14]. This technique yields large area, defect free, single crystalline samples, while affording easy control over the geometrical parameters, such as volume fraction, symmetry, and lattice length scale [15]. Interference lithography involves the transfer of an intensity pattern into a photosensitive material. This exposure step essentially binarizes the intensity distribution created via the interference into a nearly uniform material density inside some threshold isointensity contour and zero outside of it. In our case, the photoresist employed is a modified negative tone SU-8 platform [16]. Our samples consist of triangular arrays of cylindrical holes in epoxy matrix. The epoxy layer is a 6 μm thick film on a glass substrate. The average sample radius is 2 mm. Two samples have been analyzed: s1 with a cylinder radius to lattice constant ratio of $r/a = 0.1$ (4% porosity), and s2 with $r/a = 0.33$ (39% porosity). The lattice constant for both samples is $a = 1360$ nm. The scanning electron microscopy (SEM) images are shown in Figs. 1(a) and 1(b), respectively. The normal incidence transmission light diffraction pattern [Fig. 1(c)] confirms the single crystal nature and hexagonal symmetry of the structures.

We employ high resolution, angle-resolved, polarized Brillouin light scattering (BLS) to characterize phonon propagation modes in our structures. Recently, this technique was used to study acoustic properties of inhomogeneous polycrystalline bulk materials, such as systems of colloidal particles [17], concentrated ordered solutions of

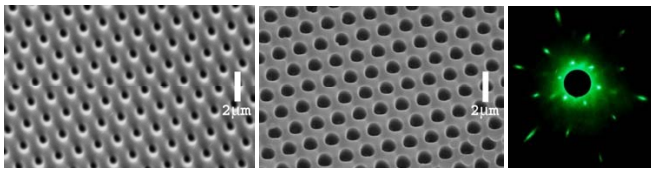

FIG. 1 (color online). SEM images of interference lithography patterned samples: (a) s1 with $r/a = 0.1$; (b) s2 with $r/a = 0.33$; (c) laser light diffraction pattern.

high molecular weight block copolymers [18,19], and lithographically patterned polymer nanostructures [20]. Our measurement geometry is described in Fig. 2. Photons with the wave vector $\vec{q}_i$ enter the sample, where they are scattered inelastically by thermal phonons, such that their wave vector becomes $\vec{q}_s$. Polarization of the incident and scattered light is maintained perpendicular to the scattering plane (s polarized) by a pair of polarizers. The orientation of the sample is adjusted in such a way that the phonon wave vector $\vec{k}$ always lies in the sample plane [Fig. 2(a)]. The magnitude of $\vec{k}$ is controlled by the scattering angle θ, while its direction in the Brillouin zone (BZ) is determined by the orientation angle φ [Fig. 2(b)]. In all our measurements $\vec{k}$ was always pointing along the Γ-M direction. The light frequency shift ω (equal to the phonon frequency) is measured using a tandem Fabry-Perot interferometer as a spectrum analyzer. A typical intensity profile consists of a very strong elastic Rayleigh peak at $\omega = 0$ and a series of symmetric Brillouin doublets at $\pm\omega$ that correspond to Stokes and anti-Stokes scattering [Fig. 3(a)]. The smallest detectable frequency shift is determined by the wings of the Rayleigh peak and by the intensity of the Brillouin doublet. In our case, it is roughly 1 GHz for the stronger glass substrate peaks and 1.5 GHz for the weaker epoxy film peaks.

To understand the effects of periodicity on the phonon propagation we first compare the spectrum of the s1 sample with that of the unpatterned photoresist film. Both spectra were taken at $|\vec{k}| = 0.0051\ \mathrm{nm}^{-1}$. Figures 3(a) and 3(b) show the scattered light intensity profiles $I(\omega,)$ for the unpatterned film and s1, respectively. Two peaks are present in the spectrum of the unpatterned sample: a high intensity peak (1) at $\omega = 4.74$ GHz coming from the glass substrate, and a less intense peak (2) at $\omega = 2.34$ GHz that corresponds to the longitudinal phonon of the polymer film. The spectrum of s1 is more complex. In addition to the most intense glass peak (1) at the same frequency, we see three less intense peaks, (2), (3), and (4), coming from various bands of the phononic crystal. The position of the lowest frequency longitudinal phonon peak (2) is shifted slightly from $\omega = 2.34$ GHz to $\omega = 2.29$ GHz, in comparison with the corresponding peak (2) of the unpatterned film, due to the decrease of the effective sound velocity in the porous polymer structure of sample s1 (4% porosity). The two new peaks (3) and (4) correspond to propagation states in the higher bands of the phononic crystal. Repeating our measurements for $|\vec{k}|$ from 0.0005 to $0.009\ \mathrm{nm}^{-1}$, we obtain complete phononic band diagrams, as shown in Figs. 3(c) and 3(d) for samples s1 and s2, respectively.

To provide interpretation of the observed modes, we calculate theoretical band diagrams and compare them with the experimental data. The finite element method (FEM), based on the weighted residual formulation [21], is employed to model the properties of the elastic structures. The FEM transforms the elastic wave equation

$$\rho\frac{\partial^2 u_i}{\partial t^2} = \nabla\cdot(\rho c_t^2\nabla u_i) + \nabla\cdot\left(\rho c_t^2\frac{\partial\vec{u}}{\partial x_i}\right) + \frac{\partial}{\partial x_i}[(\rho c_l^2 - 2\rho c_t^2)\nabla\cdot\vec{u}]$$

into a discrete generalized eigenvalue problem, where $\vec{u}$ is the displacement vector field, ρ is the density, and c_t and c_l are the transverse and longitudinal velocities, respectively. Because of the periodicity of the structure, the displacement field $\vec{u}$ satisfies Bloch's theorem. The interior air region is modeled using zero-traction boundary conditions at the air-material interface [22]. The background was taken to be epoxy with $\rho = 1.19\ \mathrm{g/cm}^3$, $c_t = 1.8$ km/s,

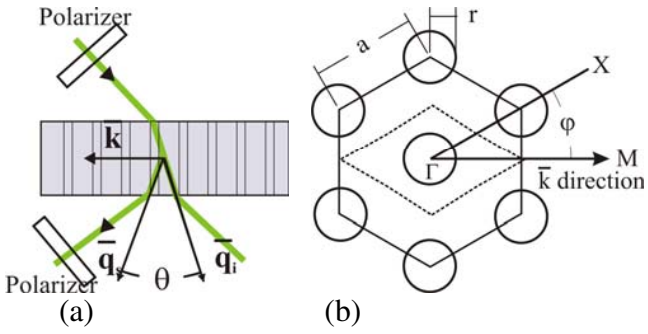

FIG. 2 (color online). BLS measurement geometry: (a) scattering plane, top view; (b) sample plane, top view. Only phonons with $\vec{k}$ essentially in the sample plane are probed.

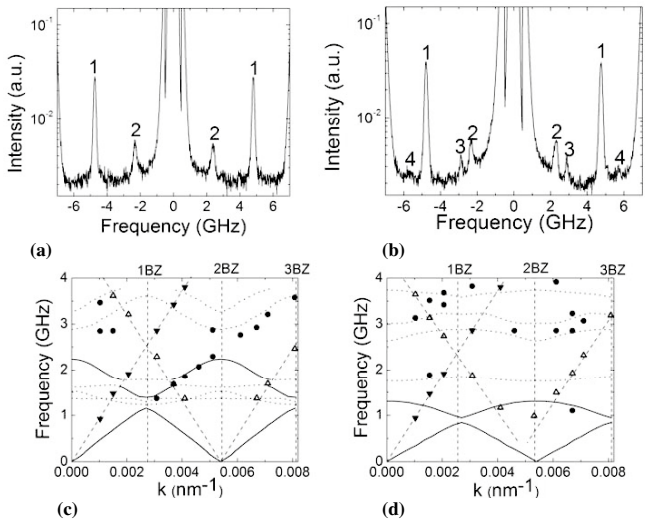

FIG. 3. BLS spectrum of the samples at $|\vec{k}| = 0.0051\ \mathrm{nm}^{-1}$: (a) unpatterned epoxy film; (b) s1 film; (c),(d) experimental and theoretical phononic band diagrams for s1 and s2 samples, respectively. Solid triangles, glass mode; open triangles, Bragg mode [18,19]; solid circles, phononic crystal modes; solid lines, theoretical quasilongitudinal modes; dotted lines, theoretical mixed modes.

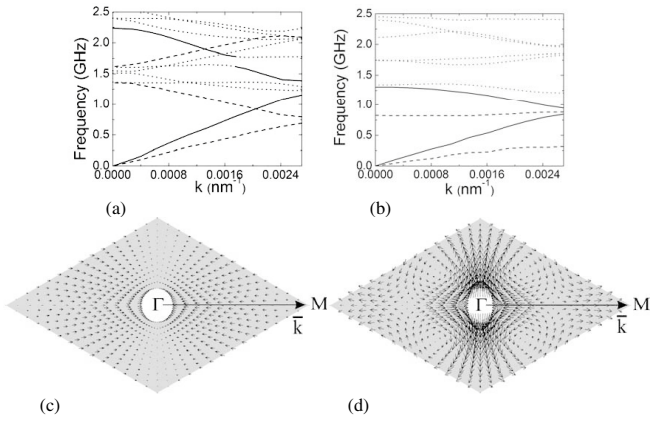

FIG. 4. (a),(b) Theoretical band diagrams for s1 and s2 samples. Solid lines represent quasilongitudinal modes; dashed line, quasitransverse modes; dotted lines, mixed modes; (c),(d) displacement field for quasilongitudinal ($|\vec{k}| = 0.0027$ nm^{-1}, $\omega = 1.16$ GHz) and mixed ($|\vec{k}| = 0.0027$ nm^{-1}, $\omega = 1.79$ GHz) modes for the s1 sample.

and $c_l = 3.1$ km/s. Figures 4(a) and 4(b) show the calculated dispersion relationship for in-plane propagation, where the displacement field $\vec{u}$ is normal to the axis of the cylinders for samples s1 and s2, respectively.

For the analysis of the scattering data it is important to understand the nature of the propagation modes in the periodic structures. In homogeneous, isotropic media there are three independent propagation modes: longitudinal (P) and two polarizations [SV (shear vertical, with displacement field perpendicular to the sample plane) and SH (shear horizontal, with displacement field in the sample plane)] of transverse waves. In contrast, in phononic crystals longitudinal and transverse waves are coupled together, such that the propagation modes are generally mixed waves. To visualize the differences among various propagation modes, we compute and compare their displacement fields [Figs. 4(c) and 4(d)]. For lower-lying modes, $\vec{u}$ is essentially either perpendicular or parallel to $\vec{k}$. We, therefore, use the terms ''quasilongitudinal waves'' and ''quasitransverse waves'' to describe these modes [Figs. 4(a) and 4(b)]. In contrast, higher band propagation modes are typically strongly mixed and cannot be approximated as either longitudinal or transverse waves. We also find that the same mode can have predominantly longitudinal displacement field character for one range of $\vec{k}$ and strongly mixed displacement field character for another range of $\vec{k}$ [Fig. 4(a)].

To identify which of the calculated modes will be actually measured experimentally, we must compute the intensities of the light scattered by different modes. Following the treatment by Landau and Lifshitz [23], the electric field in the scattered wave $\vec{E}_s$ is proportional to the vector product $[\vec{n} \times (\vec{n} \times \vec{G})]$, where $\vec{n}$ is a unit vector in the scattering direction, and the components of the vector $\vec{G}$ are given by the integral $G_i = \int \delta\varepsilon_{ik} \exp(-i\vec{k} \cdot \vec{r}) dV \cdot e_k$. Here $\vec{e}$ is a unit vector parallel to the incident electric field vector $\vec{E}_i = \vec{e} E_0 \exp(i\vec{q}_i \cdot \vec{r})$; $\delta\varepsilon_{ik}$ is the change in the electrical permittivity due to elastic deformation—$\delta\varepsilon_{ik} = a_1 u_{ik} + a_2 u_{ll} \delta_{ik}$, where $u_{ik} = \frac{1}{2}(\frac{\partial u_i}{\partial x_k} + \frac{\partial u_k}{\partial x_i})$ is a strain tensor and a_1 and a_2 are the photoelastic constants of the medium. The integration is done over the scattering volume. In the case of a plane wave propagating in a homogeneous medium, the integral for $\vec{G}$ can be evaluated analytically. For our scattering geometry we note that (i) SV modes do not scatter light; (ii) light scattered by SH modes is p polarized; (iii) light scattered by P modes is s polarized. Therefore, only the signal from longitudinal phonons will be measured.

In the case of phononic crystals, the displacement fields cannot be represented by plane waves and the integral for $\vec{G}$ must be evaluated numerically. However, the conclusions above still provide useful guidelines for the interpretation of the measured spectra. In particular, it is clear that quasilongitudinal phonons will scatter light significantly, while contributions from the quasitransverse modes will not be detected. The intensity of the mixed mode peaks will depend on their field distributions and must be evaluated separately for each mode. However, their strength will be less than the quasilongitudinal phonons peaks. For this reason, the low frequency peak (2) in the s1 spectrum [Fig. 3(b)] is more intense than peaks (3) and, especially, (4).

Figures 3(c) and 3(d) superpose experimental data points and the theoretical lines on the same graphs. Only quasilongitudinal modes (solid lines) and strongly scattering mixed modes (dotted lines) are plotted. The spectrum of sample s1 has contributions from the second quasilongitudinal mode, while the first quasilongitudinal mode is at frequencies too low to be detected. In addition, we see the signature of the strongly scattering mixed modes at the higher frequencies. The spectrum from sample s2 is very different. Because of the higher porosity, the effective sound velocity decrease is so prominent that both the first and second quasilongitudinal modes are below the detection threshold. All the higher modes are mixed. Experimental data points follow the calculated lines well, but in some places along the theoretical lines expected experimental data points appear missing. This behavior is not surprising. The scattering from the mixed modes is $\vec{k}$ dependent and relatively weak. Therefore, for some values of $\vec{k}$ it may be impossible to detect peaks even after long accumulation times. Finally, there is one mode in both the s1 and s2 spectra that does not follow any theoretical line. It is labeled as ''Bragg mode'' [18,19] and is plotted with open triangles [Figs. 3(c) and 3(d)]. To speculate on the nature of this mode, we note that its velocity is nearly equal to the glass sound velocity, while its negative dispersion is a characteristic of crystalline samples [19]. These obser-

vations strongly suggest that this mode represents a wave propagating at the film-substrate interface.

In this Letter we demonstrate that a combination of interference lithography and Brillouin light scattering constitutes a complete tool set for fabrication and characterization of hypersonic phononic crystals. We are able to create a variety of single crystalline, defect free structures, and measure their phononic band diagrams $\omega(\vec{k})$ directly. We employ FEM to perform theoretical band structure calculations and obtain very good agreement with experimental results using no fitting parameters. Our work provides foundations for experimental studies of hypersonic phononic crystals and opens a new pathway towards achieving control over phononic properties of materials.

We thank researchers at MPI for providing access to BLS facilities, in particular, to Dr. G. Tommaseo for help with the measurements. This work has benefited from several discussions with Professor J. Joannopoulos and Professor S. Johnson at MIT. Finally, we acknowledge our respective financial sources: T. G. and E. L. T., NSF Grant No. 0308133; M. M. and E. L. T., the ISN of the US ARO; C. K. U. and E. L. T., the USAF DURINT in conjunction with the University of Buffalo.

*Electronic address: taras@mit.edu

[1] M. S. Kushawa *et al.*, Phys. Rev. Lett. **71**, 2022 (1993).
[2] M. Kafesaki, M. M. Sigalas, and E. N. Economou, Solid State Commun. **96**, 285 (1995).
[3] Z. Liu *et al.*, Science **289**, 1734 (2000).
[4] R. Martinez-Sala *et al.*, Nature (London) **378**, 241 (1995).
[5] S. Yang *et al.*, Phys. Rev. Lett. **88**, 104301 (2002).
[6] L. Dhar and J. A. Rogers, Appl. Phys. Lett. **77**, 1402 (2000).
[7] A. Bartels *et al.*, Appl. Phys. Lett. **72**, 2844 (1998).
[8] Ü. Özgür, C.-W. Lee, and H. O. Everitt, Phys. Rev. Lett. **86**, 5604 (2001).
[9] A. N. Cleland, D. R. Schmidt, and C. S. Yung, Phys. Rev. B **64**, 172301 (2001).
[10] A. Urbas, Ph.D. thesis, Massachusetts Institute of Technology, 2003.
[11] E. Reed, M. Soljacic, and J. D. Joannopoulos, Phys. Rev. Lett. **90**, 203904 (2003).
[12] P. St. J. Russel, E. Martin, and A. Diez, Opt. Express **11**, 2555 (2003).
[13] G. Grynberg *et al.*, Phys. Rev. Lett. **70**, 2249 (1993).
[14] V. Berger, O. Gauthier-Lafaye, and E. Costard, J. Appl. Phys. **82**, 60 (1997).
[15] C. K. Ullal *et al.*, J. Opt. Soc. Am. A **20**, 948 (2003).
[16] S. Yang *et al.*, Chem. Mater. **14**, 2831 (2002).
[17] R. S. Penciu *et al.*, J. Chem. Phys. **118**, 5224 (2003).
[18] A. Urbas *et al.*, Phys. Rev. Lett. **90**, 108302 (2003).
[19] G. Tommaseo *et al.*, Macromolecules **37**, 5006 (2004).
[20] R. Hartschuh *et al.*, J. Polym. Sci., Part B: Polym. Phys. **42**, 1106 (2004).
[21] C. Mias, J. P. Webb, and R. L. Ferrari, IEE Proc.-Optoelectron. **146**, 111 (1999).
[22] S. Guenneau and A. B. Movchan, Arch. Ration. Mech. Anal. **171**, 129 (2004).
[23] L. D. Landau and E. M. Lifshitz, *Electrodynamics of Continuous Media* (Pergamon Press, New York, 1984).